

See discussions, stats, and author profiles for this publication at: <https://www.researchgate.net/publication/259875330>

First-Principles Study on Site Preference and $4f \rightarrow 5d$ Transitions of Ce^{3+} in $\text{Sr}_3\text{AlO}_4\text{F}$

ARTICLE in THE JOURNAL OF PHYSICAL CHEMISTRY A · JANUARY 2014

Impact Factor: 2.69 · DOI: 10.1021/jp410542y · Source: PubMed

CITATIONS

11

READS

41

9 AUTHORS, INCLUDING:



Lixin Ning

Anhui Normal University

63 PUBLICATIONS 425 CITATIONS

SEE PROFILE



Chang-Kui Duan

University of Science and Technology of China

177 PUBLICATIONS 1,810 CITATIONS

SEE PROFILE



Hongbin Liang

Sun Yat-Sen University

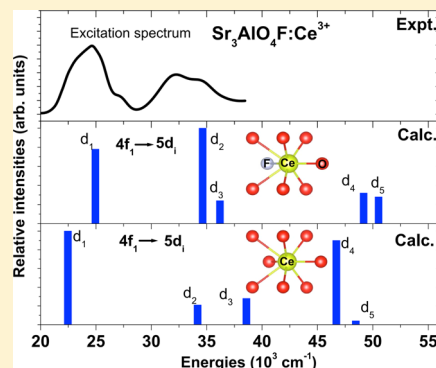
178 PUBLICATIONS 2,901 CITATIONS

SEE PROFILE

First-Principles Study on Site Preference and $4f \rightarrow 5d$ Transitions of Ce^{3+} in $\text{Sr}_3\text{AlO}_4\text{F}$ Lixin Ning,^{*,†} Yongfeng Wang,[†] Zongcui Wang,[†] Wei Jin,[†] Shizhong Huang,[†] Changkui Duan,[‡] Yongfan Zhang,[§] Wanping Chen,^{||} and Hongbin Liang^{*,||}[†]Center for Nano Science and Technology, Department of Physics, Anhui Normal University, Wuhu, Anhui 241000, China[‡]Department of Physics, University of Science and Technology of China, Hefei, Anhui, 230026, China[§]Department of Chemistry, Fuzhou University, Fuzhou, Fujian 350002, China^{||}MOE Laboratory of Bioinorganic and Synthetic Chemistry, State Key Laboratory of Optoelectronic Materials and Technologies, School of Chemistry and Chemical Engineering, Sun Yat-sen University, Guangzhou 510275, China

S Supporting Information

ABSTRACT: The local structures and $4f \rightarrow 5d$ transition energies of Ce^{3+} located on the two crystallographic strontium sites of $\text{Sr}_3\text{AlO}_4\text{F}$, with charge compensation by means of nearby sodium substitutions for strontium (Na_{Sr}') or oxygen substitutions for coordinating fluorine (O_{F}'), have been studied using the density functional theory (DFT) within the supercell model and the wave function-based embedded cluster calculations, respectively. The DFT total energy calculations show that Ce^{3+} prefers strongly to occupy the eight-coordinated (Sr2) site over the ten-coordinate (Sr1) site. On the basis of the results from embedded cluster calculations at the CASPT2 level with the spin–orbit effect, the experimentally observed excitation bands are identified in association with the charge-compensated cerium centers. Especially, the two bands observed at ~ 404 and ~ 440 nm have been both assigned to the Ce^{3+} located at the Sr2 sites but with compensation by one and two nearest-neighbor O_{F}' substitutions, respectively, rather than to the Ce^{3+} on the Sr1 and the Sr2 sites, respectively, as proposed earlier. Furthermore, the structural and electronic reasons for the red shift of the lowest $4f \rightarrow 5d$ transition caused by coordinating O_{F}' substitutions are analyzed in terms of the variations in centroid energy and crystal-field splitting of the $5d^1$ configuration with the local environment. Finally, the thermal quenching of $5d$ luminescence at relatively high Ce^{3+} concentrations is discussed on the basis of the electronic properties calculated with the hybrid DFT method.



1. INTRODUCTION

Cerium-doped oxyfluoride compounds have demonstrated great potential for use as white light-emitting diode (LED) phosphors, due to their good thermal stabilities, high quantum efficiencies, and appropriate excitation wavelengths.^{1–8} As an archetypal member of this family, cerium-doped $\text{Sr}_3\text{AlO}_4\text{F}$ ($\text{Sr}_3\text{AlO}_4\text{F}:\text{Ce}^{3+}$) exhibits a broad excitation spectrum with a intense peak at ~ 404 nm and a shoulder at ~ 440 nm, the former wavelength matching well with the output of near-UV LED chips. The emission spectrum under near-UV excitations covers a wide wavelength ranging from 400 to 650 nm, with two maxima at around 460 and 500 nm.^{1–5} These shorter- and longer-wavelength excitation or emission maxima have been assigned to $4f \rightarrow 5d$ transitions of Ce^{3+} located at the ten- and eight-coordinated strontium sites (referred to as Sr1 and Sr2 sites) of the host, respectively (cf. Figure 1), on the basis of a qualitative correlation between the lowest $4f \rightarrow 5d$ transition energy and the local coordination structure.^{4,5} However, it was recently pointed out that the bands observed in the excitation spectrum of $\text{Sr}_3\text{AlO}_4\text{F}:\text{Ce}^{3+}$ could be only due to the Ce^{3+} occupying Sr2 sites with different charge compensation

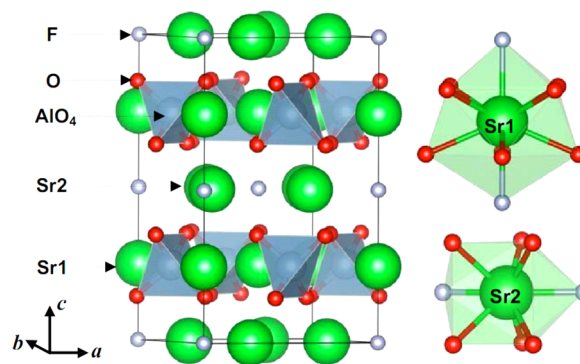


Figure 1. Schematic representations of the geometrical structure of the $\text{Sr}_3\text{AlO}_4\text{F}$ crystal and the local coordination structures of Sr1 and Sr2 atoms in the crystal.

Received: October 24, 2013

Revised: January 19, 2014

Published: January 22, 2014

Table 1. Calculated Total Energies with the DFT-PBE Method and Valences of Ce and Na with the Bond Valence Sum (BVS) Method for Ce-Doped $\text{Sr}_3\text{AlO}_4\text{F}$ Supercells^a

centers	substitutions	optimized Ce–Na distances (Å)	total energy (eV)	relative total energy (meV)	valences by BVS	
					Ce	Na
1	$\text{Ce}_{\text{Sr1}} \bullet - \text{Na}_{\text{Sr1}}'$	5.228	−931.472796	760	2.13	0.53
2	$\text{Ce}_{\text{Sr1}} \bullet - \text{Na}_{\text{Sr2}}'$	3.544	−931.849658	383	2.35	0.86
3	$\text{Ce}_{\text{Sr2}} \bullet - \text{Na}_{\text{Sr1}}'$	3.978	−931.755535	477	2.83	0.49
4	$\text{Ce}_{\text{Sr2}} \bullet - \text{Na}_{\text{Sr2}}'$	3.451	−932.129271	103	2.87	0.85
5	$\text{Ce}_{\text{Sr2}} \bullet - \text{Na}_{\text{Sr2}}'$	3.357	−932.232551	0	2.87	0.88
6	$\text{Ce}_{\text{Sr1}} \bullet - \text{O}_{\text{F}}'$		−935.663088	469	2.16	
7	$\text{Ce}_{\text{Sr2}} \bullet - \text{O}_{\text{F}}'$		−936.132057	0	2.87	
8	$\text{Ce}_{\text{Sr1}} \bullet - 2\text{O}_{\text{F}}'$		−941.527213	629	2.14	
9	$\text{Ce}_{\text{Sr2}} \bullet - 2\text{O}_{\text{F}}'$		−942.155864	0	2.79	

^aThe optimized Ce–Na distances are indicated, and the relative total energies were obtained by subtracting the lowest total energy within each group of substitutions.

mechanisms, most likely by O^{2-} replacement of F^- in the first coordination shell of Sr^{2+} . We note that the so-called “free” fluoride ions are only coordinated to larger Sr^{2+} cations and not to smaller Al^{3+} ones in $\text{Sr}_3\text{AlO}_4\text{F}$, and could presumably be easily replaced by O^{2-} to compensate for the excessive charge of Ce^{3+} residing in Sr^{2+} sites. For a further optimization of the material optical properties, it is thus necessary to obtain a better understanding of the relationship between the properties and the geometric structures using modern computational techniques. Hence, we have performed a first-principles investigation on $\text{Sr}_3\text{AlO}_4\text{F}:\text{Ce}^{3+}$ to obtain local coordination structures and $4f \rightarrow 5d$ transition energies of Ce^{3+} , and also their relationship, with various local charge compensation mechanisms considered. The results may also be useful in interpreting optical properties of other isostructural crystals, such as $\text{Sr}_2\text{BaAlO}_4\text{F}:\text{Ce}^{3+}$ and $\text{Sr}_3\text{GaO}_4\text{F}:\text{Ce}^{3+}$.^{1,2,5}

The DFT calculations with the supercell model were first performed to obtain the optimized coordination structures of Ce^{3+} substituted into the Sr1 or Sr2 sites with various charge compensation mechanisms. The Ce-centered embedded clusters were then constructed, and the $4f^1$ and $5d^1$ energy levels of Ce^{3+} were calculated using the wave function-based CASSCF/CASPT2 calculations at the spin–orbit level. Three types of local charge compensation mechanisms for the $\text{Ce}_{\text{Sr}} \bullet$ (in Kröger–Vink notation) substitution have been considered, including a nearby Na_{Sr}' replacement, a single- and a double- O_{F}' substitution in the coordination sphere of Ce^{3+} . The choice of these local charge compensation mechanisms for the present study is based on previous experimental work^{1–8} and the consideration that the point defects with net charges of opposite signs tend to get close to each other for electrostatic reasons. From the DFT total energies of Ce-doped supercells and the comparison between calculated and experimental $4f \rightarrow 5d$ transition energies, the natures of experimentally observed excitation bands were clarified in association with the charge-compensated cerium centers. The paper is organized as follows. The details of computation are described in section 2. The results for structural properties, $4f \rightarrow 5d$ transition energies, and electronic properties are presented and discussed in section 3, with the final conclusions collected in section 4.

2. COMPUTATION DETAILS

The $\text{Sr}_3\text{AlO}_4\text{F}$ host crystal was modeled by a $2 \times 2 \times 1$ supercell containing 144 atoms, in which one of the 48 Sr atoms was replaced by a Ce atom, corresponding to a chemical formula $\text{Sr}_{3-x}\text{Ce}_x\text{AlO}_4\text{F}$ with $x = 0.06$. The $\text{Sr}_3\text{AlO}_4\text{F}:\text{Ce}^{3+}$

supercells were fully relaxed using periodic DFT with the PBE functional^{9,10} as implemented in VASP.^{11,12} The Sr ($4s^2 4p^6 5s^2$), Al ($3s^2 3p^1$), O ($2s^2 2p^4$), F ($2s^2 2p^5$), Ce ($5s^2 5p^6 4f^1 5d^1 6s^2$), Na ($2p^6 3s^1$), and La ($5s^2 5p^6 5d^1 6s^2$) were treated as valence electrons, and their interactions with the cores were described by the projected augmented wave (PAW) method.¹³ The La atom was used in the case of charge compensation by a double- O_{F}' substitution in the coordination shell of Ce^{3+} , to maintain the charge neutrality of the supercell. It was located on a Sr site far way from Ce^{3+} to mimic the effect of a distant Ce^{3+} without the complication of the $4f$ electron. The convergence criteria for total energies and atomic forces were set to 10^{-6} eV and $0.01 \text{ eV } \text{\AA}^{-1}$, respectively. One k -point Γ was used to sample the Brillouin zone, with a cutoff energy of 550 eV for the plane wave basis.

On the basis of the DFT-optimized supercell structures, the Ce-centered embedded clusters were constructed, which contain the central Ce^{3+} and the coordinating O^{2-} and/or F^- ions. Their immediate surroundings within a sphere of radius 10.0 Å were represented by 496–557 embedding ab initio model potentials (AIMPs)¹⁴ at lattice sites, and the remainders of the surroundings were simulated by 46 150–48 879 point charges at lattice sites, generated with Lepetit’s method¹⁵ which produces the same electrostatic potentials as Ewald’s method.¹⁶ The wave function-based CASSCF/CASPT2 calculations with the spin–orbit effect were carried out on these embedded clusters, to obtain the $4f^1$ and $5d^1$ energy levels of Ce^{3+} , using the program MOLCAS.¹⁷ In the CASSCF calculations, a $[4f, 5d, 6s]$ complete active space has been adopted, and in the CASPT2 calculations, the dynamic correlation effects of the $5s$, $5p$, $4f$, $5d$ electrons of Ce^{3+} and the $2s$, $2p$ electrons of O^{2-} and F^- have been considered. More details on the calculation may be found in refs 18 and 19. We used a relativistic effective core potential ([Kr] core) with a $(14s10p10d8f3g)/[6s5p6d4f1g]$ Gaussian valence basis set from ref 20 for cerium, and a [He] core effective core potential with a $(5s6p1d)/[2s4p1d]$ valence basis set from ref 21 for oxygen and fluorine. Extra basis sets $(11s8p)/[1s1p]$ were added to the four Al atoms closest to the embedded clusters to improve the orthogonality of the cluster orbitals with the embedding environments.

3. RESULTS AND DISCUSSION

3.1. Structural Properties of $\text{Sr}_3\text{AlO}_4\text{F}:\text{Ce}^{3+}$. The $\text{Sr}_3\text{AlO}_4\text{F}$ crystal has a structure of tetragonal $I4/mcm$ (no. 140) symmetry, with the strontium atoms located on the $4a$ (Sr1, D_4 symmetry) and $8h$ (Sr2, C_{2v} symmetry) sites,

coordinated by eight oxygen and two fluorine atoms, and six oxygen and two fluorine atoms, respectively (Figure 1). This structure was first optimized with the DFT-PBE method, and the obtained lattice parameters are $a = 6.836$ Å and $c = 11.257$ Å, which are slightly larger (by $\leq 1\%$) than the experimental values of 6.7822 and 11.1437 Å, respectively, as determined with the synchrotron X-ray diffraction method.²² The optimized internal parameters are also in close agreement with the experimental data, with the calculated (experimental²²) values: $x_{\text{Sr}2} = 0.1687$ (0.1696), $x_{\text{O}} = 0.1423$ (0.1418), and $z_{\text{O}} = 0.6481$ (0.6496).

For Ce-doped $\text{Sr}_3\text{AlO}_4\text{F}$ supercells, five symmetrically inequivalent $\text{Ce}_{\text{Sr}i}-\text{Na}_{\text{Sr}i}'$ ($i = 1, 2$) double substitutions (centers 1–5) were first considered, which are distinguished by the five shortest Sr–Sr distances in the undoped $\text{Sr}_3\text{AlO}_4\text{F}$ supercell. Then, two $\text{Ce}_{\text{Sr}i}-\text{O}_{\text{F}}'$ substitutions within the coordination polyhedron of the Sr1 or Sr2 site (centers 6 and 7) were investigated. Two triple $\text{Ce}_{\text{Sr}i}-2\text{O}_{\text{F}}'$ substitutions within the coordination spheres of the Sr1 and Sr2 sites (centers 8 and 9) were finally studied, with the charge imbalance of the supercells compensated by a $\text{La}_{\text{Sr}2}$ replacement far away from $\text{Ce}_{\text{Sr}i}$. The distances from $\text{La}_{\text{Sr}2}$ to $\text{Ce}_{\text{Sr}1}$ and $\text{Ce}_{\text{Sr}2}$ are 7.818 and 9.150 Å, respectively, in unrelaxed supercells. In Table S1 of the Supporting Information, we list the optimized lattice parameters for these defective supercells, along with the data of the undoped one for comparison. One can see that the incorporation of charge-compensated Ce^{3+} into the supercell gives rise to very small changes (within $\pm 0.350\%$) of the volume and slightly distorts the tetragonal phase of the undoped system into phases of lower symmetries, with the deviations in the lengths and angles no larger than ± 0.028 Å and $\pm 0.117^\circ$, respectively.

Table 1 presents the total energies of the Ce-doped supercells calculated with the DFT-PBE method. The results show that, for the five centers of the $\text{Ce}_{\text{Sr}}-\text{Na}_{\text{Sr}}'$ type, the most stable ones are formed by combining $\text{Ce}_{\text{Sr}2}$ and $\text{Na}_{\text{Sr}2}'$ substitutions, i.e., centers 4 and 5, with the latter being slightly more stable than the former due to its shorter Ce–Na distance. All other centers of this type are relatively unstable, and the instability is largest for the $\text{Ce}_{\text{Sr}1}-\text{Na}_{\text{Sr}1}'$ substitution (center 1). The relative stability of these centers can be qualitatively understood by comparing the formal valences of Ce^{3+} and Na^+ with those derived from their coordination structures using the bond valence sum (BVS) method.²³ The calculated BVS values for Ce and Na in these defective supercells are listed in the last two columns of Table 1. We see that the BVS values for the two ions on the Sr2 sites are 2.83–2.87 and 0.85–0.88, respectively, both much closer to their respective formal values than those (2.13–2.35 and 0.49–0.53, respectively) obtained for the two ions on the Sr1 sites. This shows the greater stability of Ce or Na on the Sr2 site than on the Sr1 site, consistent with the results of DFT total energy calculations. For the two $\text{Ce}_{\text{Sr}i}-\text{O}_{\text{F}}'$ and the two $\text{Ce}_{\text{Sr}i}-2\text{O}_{\text{F}}'$ ($i = 1, 2$) centers, Table 1 shows again that the occupation of Ce^{3+} on the Sr2 site is more stable than on the Sr1 site, which can be explained similarly by the BVS results of Ce on the two strontium sites (as shown in the table).

The optimized coordination structures of Ce^{3+} in the most stable centers of each type (centers 5, 7, and 9) are depicted in Figure 2b–d, respectively, together with that of Sr^{2+} on the Sr2 site of $\text{Sr}_3\text{AlO}_4\text{F}$ (Figure 2a) for comparison. The values of bond lengths and site symmetries are also indicated. Figure 2b shows that, for $\text{Ce}_{\text{Sr}2}-\text{Na}_{\text{Sr}2}'$ (center 5), the coordination

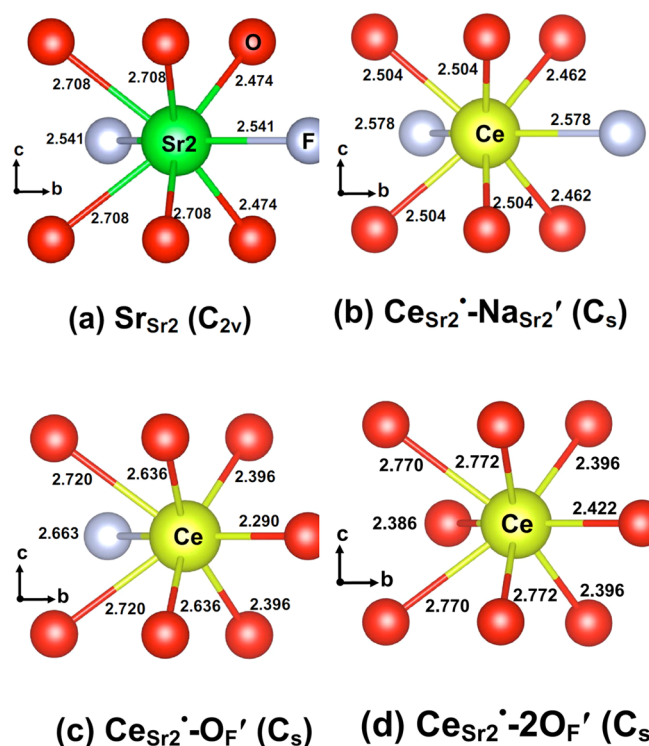


Figure 2. Optimized local structures of Sr^{2+} and Ce^{3+} on the Sr2 sites of $\text{Sr}_3\text{AlO}_4\text{F}$. The values of bond distances and the point group symmetries are indicated.

structure is distorted with respect to that of Sr^{2+} , with the four distant and the two close oxygens moving inward by 0.204 and 0.012 Å, respectively, and the two fluorines moving outward by 0.037 Å. The average distance from Ce^{3+} to the coordinating anions is decreased by 0.096 Å, with the polyhedron size reduced by 10.796%. For $\text{Ce}_{\text{Sr}2}-\text{O}_{\text{F}}'$ (center 7, Figure 2c), the bond lengths of $\text{Ce}_{\text{Sr}2}-\text{O}_{\text{F}}'$ and $\text{Ce}_{\text{Sr}2}-\text{F}$ are shorter by 0.251 Å and longer by 0.122 Å, respectively, than that of $\text{Sr}2-\text{F}$ in $\text{Sr}_3\text{AlO}_4\text{F}$ (Figure 2a). Four of the remaining six coordinating oxygens are shifted inward by 0.07–0.08 Å, and the other two are shifted away by 0.012 Å. The average bond length is decreased by 0.051 Å, and the size of the coordination polyhedron is reduced by 6.408%. For $\text{Ce}_{\text{Sr}2}-2\text{O}_{\text{F}}'$ (center 9, Figure 2d), it is interesting to note that, although the size reduction of the coordination polyhedron is relatively small (by 2.956%) with a slight decrease (by 0.022 Å) in the average bond length, the changes of the individual bond lengths are pronounced, when compared with those of the undoped system. The two $\text{Ce}_{\text{Sr}2}-\text{O}_{\text{F}}'$ bond lengths are shortened by 0.155 and 0.119 Å from that of $\text{Sr}2-\text{F}$ (Figure 2a), whereas for the other six $\text{Ce}_{\text{Sr}2}-\text{O}$ bond lengths, four are lengthened by 0.062–0.064 Å and the other two shortened by 0.078 Å. To summarize, the $\text{Ce}_{\text{Sr}2}$ substitution causes an anisotropic distortion of the coordination structure of the dopant site, which is especially pronounced for the case with one coordinating O_{F}' substitution. These structural changes could be attributed to the smaller ionic radius of Ce^{3+} (1.143 Å) than Sr^{2+} (1.26 Å) in the 8-fold coordination,²⁴ and the additional electrostatic attraction of Ce^{3+} with O^{2-} compared to that of Sr^{2+} with F^- or O^{2-} , due to the excessive positive and/or negative charge. The coordination structures of Ce^{3+} in the other Ce centers considered in the present work are displayed in Figure S1 of the Supporting Information. We note from the

Table 2. Calculated Energy Levels (cm^{-1}) of $4f^1$ and $5d^1$ Configurations for Charge-Compensated Ce^{3+} Centers in $\text{Sr}_3\text{AlO}_4\text{F}$, Using the CASSCF/CASPT2 Method with the Spin–Orbit Coupling

	center 1 $\text{Ce}_{\text{Sr1}}^{\bullet}-\text{Na}_{\text{Sr1}}'$	center 2 $\text{Ce}_{\text{Sr1}}^{\bullet}-\text{Na}_{\text{Sr2}}'$	center 3 $\text{Ce}_{\text{Sr2}}^{\bullet}-\text{Na}_{\text{Sr1}}'$	center 4 $\text{Ce}_{\text{Sr2}}^{\bullet}-\text{Na}_{\text{Sr2}}'$	center 5 $\text{Ce}_{\text{Sr2}}^{\bullet}-\text{Na}_{\text{Sr2}}'$	center 6 $\text{Ce}_{\text{Sr1}}^{\bullet}-\text{O}_\text{F}'$	center 7 $\text{Ce}_{\text{Sr2}}^{\bullet}-\text{O}_\text{F}'$	center 8 $\text{Ce}_{\text{Sr1}}^{\bullet}-2\text{O}_\text{F}'$	center 9 $\text{Ce}_{\text{Sr2}}^{\bullet}-2\text{O}_\text{F}'$
$4f_1$	0	0	0	0	0	0	0	0	0
$4f_2$	228	126	181	112	40	165	626	1012	581
$4f_3$	502	958	453	593	663	388	828	2016	1105
$4f_4$	2290	2251	2214	2215	2153	2149	2180	2334	2311
$4f_5$	2369	2525	2415	2327	2316	2458	2642	2994	2547
$4f_6$	2585	2702	2570	2696	2814	2700	3476	3839	3179
$4f_7$	3050	3656	2933	3092	2903	2783	3635	5015	4436
$5d_1$	32477	33672	29093	28499	29357	32196	24951	31064	22469
$5d_2$	38538	34528	36824	37672	36380	35716	34634	36482	34181
$5d_3$	39026	37280	38642	39773	39066	36914	36197	38114	38584
$5d_4$	43895	38288	40623	40942	42159	41842	49166	39451	46705
$5d_5$	45853	52096	54774	55010	53366	46863	50519	49318	48461

figure that, although the average bond length (2.514 Å) in center 4 is very close to that (2.511 Å) of center 5 (Figure 2b), the former center has a coordination structure more distorted than the latter, consistent with the relative stability of the two centers, as revealed by DFT total-energy calculations.

3.2. $4f \rightarrow 5d$ Transition Energies of Ce^{3+} . On the basis of the DFT-optimized structures for the various $\text{Sr}_3\text{AlO}_4\text{F}:\text{Ce}^{3+}$ supercells, Ce-centered embedded clusters were constructed with their environments represented by AIMP and point charges at lattice sites. The wave function-based CASSCF/CASPT2 calculations were then conducted to obtain the energies of $4f^1$ and $5d^1$ levels. The results with and without the spin–orbit coupling are listed in Table 2 and Table S2 of the Supporting Information, respectively. A comparison of the data in the two tables shows that, besides its expected importance for the $4f^1$ levels, the inclusion of the spin–orbit effect increases the $5d^1$ level energies uniformly by around 1000 cm^{-1} for the nine centers under study, which has also been observed in Ce^{3+} -doped $\text{Y}_3\text{Al}_5\text{O}_{12}$ and Lu_2SiO_5 systems.^{18,19} From Table 2, one sees that, for all of the centers, the seven $4f^1$ levels fall into two groups (i.e., $4f_{1-3}$ and $4f_{4-7}$ levels) with a separation of $2322\text{--}2557 \text{ cm}^{-1}$, which can be linked with the $^7F_{5/2}$ and $^7F_{7/2}$ multiplet terms of Ce^{3+} split by the spin–orbit interaction. The lowest ($5d_1$) levels of Ce^{3+} on the Sr1 sites lie in the energy range $31\,000\text{--}33\,700 \text{ cm}^{-1}$ with respect to the $4f_1$ ground levels, much higher than those ($22\,400\text{--}29\,400 \text{ cm}^{-1}$) of Ce^{3+} on the Sr2 sites.

To facilitate comparison with experimental excitation band maxima, the calculated $4f_i \rightarrow 5d_i$ ($i = 1, 5$) transitions for charge-compensated Ce^{3+} are schematically represented in Figures 3 and 4. The relative absorption intensities were calculated using the wave functions and energies at the spin–orbit level in the expression $e^{-E_{if}/kT} \Delta E \sum_q |\langle 4f_i | D_q | 5d_i \rangle|^2$, where the summation is over the polarization q ($q = 0, \pm 1$). From Figure 3, one can see that there are no significant contributions from the $\text{Ce}_{\text{Sr1}}^{\bullet}-\text{Na}_{\text{Sr1}}'$ ($i = 1, 2$) centers (Figure 3b–f) to the experimental excitation bands A–C in Figure 3a. This indicates that these excitation bands are not due to the Ce^{3+} on the Sr1 or Sr2 sites with local coordination environments similar to those in the pure host. In contrast, Figure 4 clearly shows that the excitation bands A ($\sim 440 \text{ nm}$) and B ($\sim 404 \text{ nm}$) can be assigned to the lowest $4f_1 \rightarrow 5d_1$ transitions of the $\text{Ce}_{\text{Sr2}}^{\bullet}-2\text{O}_\text{F}'$ (Figure 4e) and $\text{Ce}_{\text{Sr2}}^{\bullet}-\text{O}_\text{F}'$ (Figure 4c) centers, with deviations of 260 and 200 cm^{-1} , respectively. Moreover, the lower intensity of band A than that of band B in the excitation

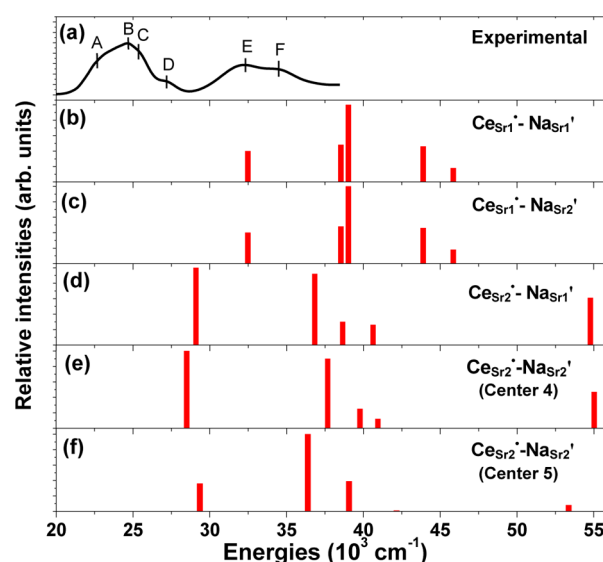


Figure 3. Schematic diagram for the calculated energies and relative oscillator strengths of $4f_i \rightarrow 5d_i$ ($i = 1\text{--}5$) transitions (in order of increasing energy) of $\text{Ce}_{\text{Sri}}^{\bullet}-\text{Na}_{\text{Sri}}'$ ($i = 1, 2$) centers in $\text{Sr}_3\text{AlO}_4\text{F}$. The experimental excitation spectrum is also included for comparison.

spectrum suggests that the formation of the $\text{Ce}_{\text{Sr2}}^{\bullet}-\text{O}_\text{F}'$ center is more favored than the $\text{Ce}_{\text{Sr2}}^{\bullet}-2\text{O}_\text{F}'$ center. Band C in Figure 4a may arise from the $4f_1 \rightarrow 5d_1$ transitions of $\text{Ce}_{\text{Sr2}}^{\bullet}-\text{O}_\text{F}'$ centers with additional defects in the second coordination sphere, in view of its close proximity in energy to band B. Band D could be at least partly due to the $4f_1 \rightarrow 5d_1$ transitions of a small amount of $\text{Ce}_{\text{Sr2}}^{\bullet}-\text{Na}_{\text{Sr2}}'$ centers (Figure 3d–f) present in $\text{Sr}_3\text{AlO}_4\text{F}:\text{Ce}^{3+}$, as indicated from a comparison of the calculated and experimental transition energies. Bands E and F may have contributions from the $4f_1 \rightarrow 5d_1$ transitions of $\text{Ce}_{\text{Sr1}}^{\bullet}-\text{O}_\text{F}'$ (Figure 4b) and $\text{Ce}_{\text{Sr1}}^{\bullet}-2\text{O}_\text{F}'$ (Figure 4d) centers, and also from the second lowest $4f_1 \rightarrow 5d_2$ transitions of $\text{Ce}_{\text{Sr2}}^{\bullet}-\text{O}_\text{F}'$ and $\text{Ce}_{\text{Sr2}}^{\bullet}-2\text{O}_\text{F}'$ centers.

The above comparisons provide direct evidence that the excitation band maximum at $\sim 404 \text{ nm}$ and the shoulder at $\sim 440 \text{ nm}$ are both due to the $4f_1 \rightarrow 5d_1$ transitions of Ce^{3+} on the Sr2 sites, but with one and two O^{2-} ions on the coordinating F^- sites, respectively. This assignment is also consistent with the results of DFT total-energy calculations that the Ce^{3+} ions prefer to occupy the Sr2 sites over the Sr1 sites with the same type of charge compensation mechanism. The

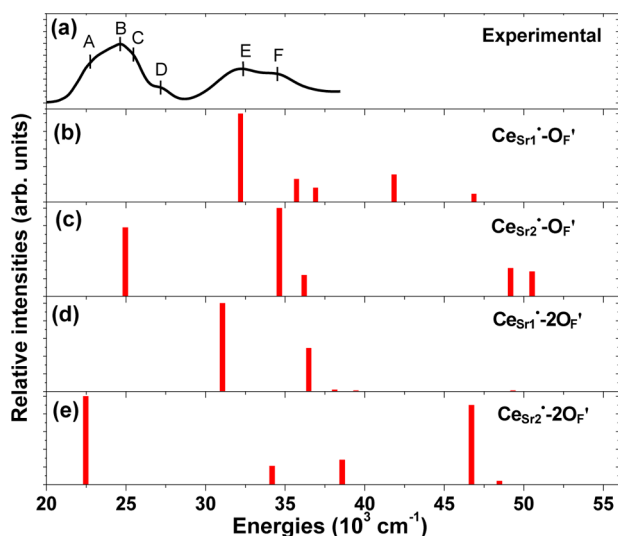


Figure 4. Schematic diagram for the calculated energies and relative oscillator strengths of $4f_i \rightarrow 5d_i$ ($i = 1-5$) transitions (in order of increasing energy) of $\text{Ce}_{\text{Sr}i'}-\text{O}_{\text{F}}'$ and $\text{Ce}_{\text{Sr}i'}-2\text{O}_{\text{F}}'$ ($i = 1, 2$) centers in $\text{Sr}_3\text{AlO}_4\text{F}$. The experimental excitation spectrum is also included for comparison.

occurrence of charge-compensating O_{F}' in the coordination polyhedron of the dopant Ce^{3+} might be expected from the fact that the oxygen from the precursor CeO_2 has a high solubility in $\text{Sr}_3\text{AlO}_4\text{F}:\text{Ce}^{3+}$ during the synthesizing process and is difficult to distinguish from fluorine by X-ray diffraction techniques.²⁵

For the lowest $4f_1 \rightarrow 5d_1$ transitions of Ce^{3+} on the Sr2 sites (centers 5, 7, and 9 in Table 2), our calculations show that an O_{F}' substitution in the coordination polyhedron leads to a decrease of $\sim 4400 \text{ cm}^{-1}$ in the transition energy, and a second coordinating O_{F}' replacement to a further reduction of $\sim 2480 \text{ cm}^{-1}$. These energy shifts can be explained by the variations of the $5d_1$ centroid energy (ce) and crystal-field splitting (cfs) with the local coordination structure. The $4f_1 \rightarrow 5d_1$ transition energy may be expressed as $\Delta E(4f_1 \rightarrow 5d_1) = \Delta E_{\text{ce}}(4f_1 \rightarrow 5d_1) - \Delta E_{\text{cfs}}(5d_1)$, where $\Delta E_{\text{ce}}(4f_1 \rightarrow 5d_1)$ denotes the energy difference between the $5d_1$ centroid and the $4f_1$ ground level, and $\Delta E_{\text{cfs}}(5d_1)$ is the relative energy of the $5d_1$ level with respect to the $5d_1$ centroid. From the data in Table 2, we obtain the values of $\Delta E_{\text{ce}}(4f_1 \rightarrow 5d_1)$ as 40 068, 39 093, and 38 080 cm^{-1} for $\text{Ce}_{\text{Sr}2'}-\text{Na}_{\text{Sr}2'}$ (center 5), $\text{Ce}_{\text{Sr}2'}-\text{O}_{\text{F}}'$ (center 7), and $\text{Ce}_{\text{Sr}2'}-2\text{O}_{\text{F}}'$ (center 9), respectively, indicating an average decrease of $\sim 1000 \text{ cm}^{-1}$ by each O_{F}' substitution. This decrease can be understood either by the much larger polarizability of O^{2-} than F^- according to the ligand polarization model,^{26,27} or by the O_{F}' -induced enhancement of covalency effects as revealed by a reduction in the charge on Ce^{3+} 5d orbitals from Mulliken population analysis of the $5d_i$ eigenfunctions, according to the covalency model.²⁸

On the other hand, the derived value of $\Delta E_{\text{cfs}}(5d_1)$ increases significantly, from 10 708 cm^{-1} for center 5, to 14 143 cm^{-1} for center 7, and to 15 611 cm^{-1} for center 9. This is consistent with the results of DFT geometrical optimizations that the distortion of the coordination structure of Ce^{3+} increases also in the same order (Figure 2), because a greater distortion is expected to yield a larger crystal-field splitting of the $5d_1$ configuration. These structural effects are much stronger than the above electronic effects in determining the red shift of the

$4f_1 \rightarrow 5d_1$ transition as a result of coordinating O_{F}' substitutions.

3.3. Electronic Properties of $\text{Sr}_3\text{AlO}_4\text{F}:\text{Ce}^{3+}$. Experimentally,⁶ it was observed that thermal quenching of the Ce^{3+} 5d luminescence upon excitation at $\sim 400 \text{ nm}$ becomes significant at high cerium concentrations. This was tentatively explained by an increased energy transfer from high-energy to low-energy centers, which were assumed to have large thermally stimulated 5d ionization efficiencies to the conduction band as a result of the reduced band gap due to O_{F}' replacements. To examine this, we have calculated total and orbital-projected density of states (DOS) for the undoped and the doped supercells of the most stable $\text{Ce}_{\text{Sr}2'}-\text{Na}_{\text{Sr}2'}$, $\text{Ce}_{\text{Sr}2'}-\text{O}_{\text{F}}'$, and $\text{Ce}_{\text{Sr}2'}-2\text{O}_{\text{F}}'$ substitutions using DFT with the hybrid PBE0 functional,²⁹ which has been shown to improve the calculated band gap when compared to the pure PBE functional.³⁰ The results show that, for pure $\text{Sr}_3\text{AlO}_4\text{F}$ (Figure 5a), the top of the valence band

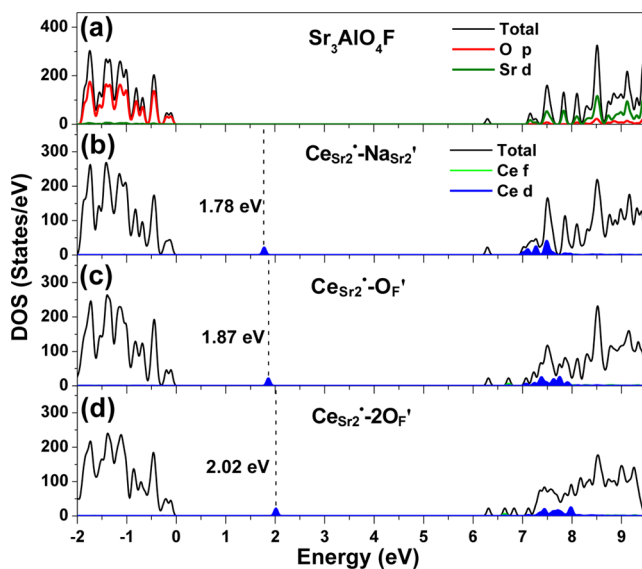


Figure 5. Total and orbital-projected DOS for the pure and Ce-doped $\text{Sr}_3\text{AlO}_4\text{F}$ crystals using DFT with the PBE0 functional. The energies of the occupied Ce^{3+} 4f bands with respect to the valence band maximum of the host are indicated in the legends. The occupied Ce^{3+} 4f states are indicated by the dashed lines.

and the bottom of the conduction band are predominantly formed by O 2p states and Sr 4d states, respectively. The conduction band edge is constituted by a small peak at 6.30 eV above the Fermi level, which is mainly composed of s-character states of Sr and O atoms.

For the doped supercells (Figure 5b–d), the incorporation of Ce into $\text{Sr}_3\text{AlO}_4\text{F}$ leads to the formation of occupied Ce^{3+} 4f states in the band gap (indicated by the dash lines in the figures), each corresponding to a lone 4f electron. A comparison of these figures shows that the value of the host band gap is almost unchanged for the three different charge compensation mechanisms. Only the gap (ΔE_{4f}) between the occupied 4f state and the top of the host valence band increases slightly from 1.78 eV for $\text{Ce}_{\text{Sr}2'}-\text{Na}_{\text{Sr}2'}$, to 1.87 eV for $\text{Ce}_{\text{Sr}2'}-\text{O}_{\text{F}}'$, and to 2.02 eV for $\text{Ce}_{\text{Sr}2'}-2\text{O}_{\text{F}}'$. Combining these data with the calculated $4f_1 \rightarrow 5d_1$ transition energies of the centers (Table 2) and the almost constant band gap value of the host, we see that the increase of the number of O_{F}' substitutions does not lead to a narrowing of the gap between the lowest

Ce³⁺ 5d₁ level and the bottom of the conduction band, and thus not to an enhancement of 5d thermal ionization efficiency. Therefore, the low-energy centers with very strong thermal quenching, as observed experimentally at relatively high Ce³⁺ concentrations (Figure 2b in ref 7), were not formed from Ce_{Sr2}[•] with charge compensation by coordinating O_F' and might correspond to centers other than those considered in this work.

4. CONCLUSIONS

First-principles calculations have been performed on the 4f → 5d transition energies of Ce³⁺ located on the ten-coordinated Sr1 and the eight-coordinated Sr2 sites of Sr₃AlO₄F, with local charge compensation by nearby Na_{Sr}' or coordinating O_F' substitutions, to better understand optical properties of the material. The DFT-PBE method with the supercell model was first employed to optimize the local structures of Ce³⁺, based on which Ce-centered embedded clusters were constructed and the wave function-based CASSCF/CASPT2 calculations with the spin-orbit coupling were then carried out to obtain the energies of Ce³⁺ 4f¹ and 5d¹ levels. It was found that the incorporation of charge-compensated Ce³⁺ into Sr₃AlO₄F causes an anisotropic distortion of its local structure, which is especially pronounced for the compensation by a coordinating O_F' substitution. It was revealed from DFT supercell total-energy calculations that the dopant Ce³⁺ prefers to occupy the smaller Sr2 sites over the larger Sr1 sites with the same type of charge compensation mechanism.

From comparison between the calculated and experimental 4f → 5d transition energies, the experimental excitation bands have been identified in association with the Ce³⁺ sites. In particular, the two excitation bands at ~404 and ~440 nm have been both assigned to the Ce³⁺ located on Sr2 sites but with one and two O_F' replacements, respectively, in the first coordination sphere, rather than to the Ce³⁺ on the Sr1 and the Sr2 sites, respectively, as proposed earlier. Moreover, the structural and electronic reasons behind the red shifts of the lowest 4f₁ → 5d₁ transition as induced by O_F' substitutions have been analyzed in terms of the variations of centroid energy and crystal-field splitting of the 5d¹ configuration. Finally, the experimentally observed thermal quenching of 5d luminescence at relatively high Ce³⁺ concentrations has been discussed on the basis of the calculated electronic properties of Ce-doped supercells with the hybrid DFT method and the calculated 4f₁ → 5d₁ transition energies, with the finding that the low-energy centers exhibiting strong thermal quenching are not due to Ce³⁺ on the Sr2 sites with O_F' substitutions in the coordination polyhedron. The present work also demonstrates the usefulness of first-principles calculations in clarifying the relationship between local structures and spectroscopic properties in cerium-doped optical materials.

■ ASSOCIATED CONTENT

Supporting Information

Calculated lattice constants for Ce-doped Sr₃AlO₄F supercells (Table S1), calculated 4f¹ and 5d¹ level energies with the CASSCF/CAPT2 method (Table S2), and local structures of the dopant Ce³⁺ (Figure S2). This material is available free of charge via the Internet at <http://pubs.acs.org>.

■ AUTHOR INFORMATION

Corresponding Authors

*L. Ning: e-mail, ninglx@gmail.com; tel, +86 553 3869748; fax, +86 553 3869748.

*H. Liang: e-mail, cesbin@mail.sysu.edu.cn; tel, +86 20 84113695; fax, +86 20 84111038.

Notes

The authors declare no competing financial interest.

■ ACKNOWLEDGMENTS

This work has been supported by the National Science Foundation of China (Grant nos. 11174005, 21171176, 11274299, 21373048, and U1232108). W.J. acknowledges support from the funding for postdoctoral research program of Anhui Normal University (Grant no. 161-071218).

■ REFERENCES

- (1) Im, W. B.; George, N.; Kurzman, J.; Brinkley, S.; Mikhailovsky, A.; Hu, J.; Chmelka, B. F.; DenBaars, S. P.; Seshadri, R. Efficient and Color-Tunable Oxyfluoride Solid Solution Phosphors for Solid-State White Lighting. *Adv. Mater.* **2011**, 23, 2300–2305.
- (2) Denault, K. A.; George, N. C.; Paden, S. R.; Brinkley, S.; Mikhailovsky, A. A.; Neufeind, J.; DenBaars, S. P.; Seshadri, R. A Green-Yellow Emitting Oxyfluoride Solid Solution Phosphor Sr₂Ba-(AlO₄F)_{1-x}(SiO₅)_x:Ce³⁺ for Thermally Stable, High Color Rendition Solid State White Lighting. *J. Mater. Chem.* **2012**, 22, 18204–18213.
- (3) Im, W. B.; Brinkley, S.; Hu, J.; Mikhailovsky, A.; DenBaars, S. P.; Seshadri, R. Sr_{2.975-x}Ba_xCe_{0.025}AlO₄F: A Highly Efficient Green-Emitting Oxyfluoride Phosphor for Solid State White Lighting. *Chem. Mater.* **2010**, 22, 2842–2849.
- (4) Chen, W.; Liang, H.; Ni, H.; He, P.; Su, Q. Chromaticity-Tunable Emission of Sr₃AlO₄F:Ce³⁺ Phosphors: Correlation with Matrix Structure and Application in LEDs. *J. Electrochem. Soc.* **2010**, 157, J159–J163.
- (5) Chen, W.; Liang, H.; Han, B.; Zhong, J.; Su, Q. Emitting-Color Tunable Phosphors Sr₃GaO₄F:Ce³⁺ at Ultraviolet Light and Low-Voltage Electron Beam Excitation. *J. Phys. Chem. C* **2009**, 113, 17194–17199.
- (6) Setlur, A. A.; Porob, D. G.; Happek, U.; Brik, M. G. Concentration Quenching in Ce³⁺-Doped LED Phosphors. *J. Lumin.* **2013**, 133, 66–68.
- (7) Setlur, A. A.; Radkov, E. V.; Henderson, C. S.; Her, J.; Srivastava, A. M.; Karkada, N.; Satya Kishore, M.; Kumar, N. P.; Aesram, D.; Deshpande, A.; Kolodin, B.; Grigorov, L. S.; Happek, U. Energy-Efficient, High-Color-Rendering LED Lamps Using Oxyfluoride and Fluoride Phosphors. *Chem. Mater.* **2010**, 22, 4076–4082.
- (8) Fang, Y.; Li, Y. Q.; Qiu, T.; Delsing, A. C. A.; de With, G.; Hintzen, H. T. Photoluminescence Properties and Local Electronic Structures of Rare Earth-Activated Sr₃AlO₄F. *J. Alloys Compd.* **2010**, 496, 614–619.
- (9) Perdew, J. P.; Burke, K.; Ernzerhof, M. Generalized Gradient Approximation Made Simple. *Phys. Rev. Lett.* **1996**, 77, 3865–3868.
- (10) Perdew, J. P.; Burke, K.; Ernzerhof, M. Generalized Gradient Approximation Made Simple. *Phys. Rev. Lett.* **1997**, 78, 1396.
- (11) Kresse, G.; Furthmüller, J. Efficient Iterative Schemes for Ab Initio Total-Energy Calculations Using a Plane-Wave Basis Set. *Phys. Rev. B* **1996**, 54, 11169–11186.
- (12) Kresse, G.; Joubert, D. From Ultrasoft Pseudopotentials to the Projector Augmented-Wave Method. *Phys. Rev. B* **1999**, 59, 1758–1775.
- (13) Blöchl, P. E. Projector Augmented-Wave Method. *Phys. Rev. B* **1994**, 50, 17953–17979.
- (14) Barandiarán, Z.; Seijo, L. The Abinitio Model Potential Representation of the Crystalline Environment. Theoretical Study of the Local Distortion on NaCl:Cu⁺. *J. Chem. Phys.* **1988**, 89, 5739–5748.

- (15) Gellé, A.; Lepetit, M. Fast Calculation of the Electrostatic Potential in Ionic Crystals by Direct Summation Method. *J. Chem. Phys.* **2008**, *128*, 244716.
- (16) Ewald, P. P. The Computation of Optical and Electrostatic Lattice Potentials. *Ann. Phys.-Paris* **1921**, *64*, 253–287.
- (17) Karlström, G.; Lindh, R.; Malmqvist, P.-Å.; Roos, B. O.; Ryde, U.; Veryazov, V.; Widmark, P. O.; Cossi, M.; Schimmelpfennig, B.; Neogrady, P.; Seijo, L. Molcas: a Program Package for Computational Chemistry. *Comput. Mater. Sci.* **2003**, *28*, 222–239.
- (18) Muñoz-García, A. B.; Pascual, J. L.; Barandiarán, Z.; Seijo, L. Structural Effects and 4f-5d Transition Shifts Induced by La Codoping in Ce-Doped Yttrium Aluminum Garnet: First-Principles Study. *Phys. Rev. B* **2010**, *82*, 064114.
- (19) Ning, L.; Lin, L.; Li, L.; Wu, C.; Duan, C.; Zhang, Y.; Seijo, L. Electronic Properties and 4f→5d Transitions in Ce-Doped Lu₂SiO₅: A Theoretical Investigation. *J. Mater. Chem.* **2012**, *22*, 13723–13731.
- (20) Seijo, L.; Barandiarán, Z.; Ordejón, B. Transferability of Core Potentials to f and d States of Lanthanide and Actinide Ions. *Mol. Phys.* **2003**, *101*, 73–80.
- (21) Barandiarán, Z.; Seijo, L. The Ab initio Model Potential Method. Cowan-Griffin Relativistic Core Potentials and Valence Basis Sets from Li (Z=3) to La (Z=57). *Can. J. Chem.* **1992**, *70*, 409–415.
- (22) Vogt, T.; Woodward, P. M.; Hunter, B. A.; Prodjosantoso, A. K.; Kennedy, B. J. Sr₃MO₄F (M=Al,Ga)-A New Family of Ordered Oxyfluorides. *J. Solid State Chem.* **1999**, *144*, 228–231.
- (23) Brese, N. E.; O’Keeffe, M. Bond-Valence Parameters for Solids. *Acta Crystallogr.* **1991**, *B47*, 192–197.
- (24) Shannon, R. D. Revised Effective Ionic Radii and Systematic Studies of Interatomic Distances in Halides and Chalcogenides. *Acta Crystallogr. A* **1976**, *32*, 751–767.
- (25) Du, L. S.; Samoson, A.; Tuherm, T.; Grey, C. P. ¹⁹F/²³Na Double Resonance MAS NMR Study of Oxygen/Fluorine Ordering in the Oxyfluoride Na₅W₃O₉F₅. *Chem. Mater.* **2000**, *12*, 3611–3616.
- (26) Judd, B. R. Correlation Crystal Fields for Lanthanide Ions. *Phys. Rev. Lett.* **1977**, *39*, 242–244.
- (27) Morrison, C. A. Host Dependence of the Rare-Earth Ion Energy Separation 4f^N–4f^{N-1}nl. *J. Chem. Phys.* **1980**, *72*, 1001–1002.
- (28) Aull, B. F.; Jenssen, H. P. Impact of Ion-Host Interactions on the 5d-to-4f Spectra of Lanthanide Rare-Earth-Metal Ions. I. A Phenomenological Crystal-Field Model. *Phys. Rev. B* **1986**, *34*, 6640–6646.
- (29) Perdew, J. P.; Ernzerhof, M.; Burke, K. Rationale for Mixing Exact Exchange with Density Functional Approximations. *J. Chem. Phys.* **1996**, *105*, 9982.
- (30) Alkauskas, A.; Broqvist, P.; Pasquarello, A. Defect Levels through Hybrid Density Functionals: Insights and Applications. *Phys. Status Solidi B* **2011**, *248*, 775–789.